Pressure-temperature phase diagram of Ti_2O_3 and physical properties in the golden Th_2S_3-type phase

Sergey V. Ovsyannikov,[1,*] Xiang Wu,[2] Alexander E. Karkin,[3] Vladimir V. Shchennikov,[4] and Geeth M. Manthilake[1]

[1]*Bayerisches Geoinstitut, Universität Bayreuth, Universitätsstrasse 30, Bayreuth D-95447, Germany*

[2]*School of Earth and Space Sciences, Peking University, Beijing 100871, China*

[3]*Research Department on Nuclear Reactor, Institute of Metal Physics, Russian Academy of Sciences, Urals Division, GSP-170, 18 S. Kovalevskaya Str., Yekaterinburg 620041, Russia*

[4]*High Pressure Group, Institute of Metal Physics, Russian Academy of Sciences, Urals Division, GSP-170, 18 S. Kovalevskaya Str., Yekaterinburg 620041, Russia*

(Received 18 September 2011; revised manuscript received 14 April 2012; published 16 July 2012)

In this paper, the pressure and temperature conditions of the synthesis of a recently discovered golden Th_2S_3-type phase of titanium sesquioxide (Ti_2O_3) are studied, along with its physical properties. In combined x-ray diffraction and Raman high-pressure studies at room-temperature we found signatures of an isostructural transition at pressures near ∼8–10 GPa. This finding was addressed to the well-known isostructural semiconductor-semimetal transition that occurs at ambient pressure near 400–450 K. Above ∼10 GPa the golden phase was synthesized under appropriate heating. Based on both *in-situ* high-pressure high-temperature (HP-HT) studies in diamond anvil cells and *ex-situ* studies on samples synthesized at HP-HT conditions in multianvil cells, we constructed a pressure-temperature phase diagram of Ti_2O_3 for the first time. The samples of the golden polymorph were examined by Raman, absorption, and reflectance spectroscopy as well as by measurements of electrical resistivity, Hall effect, thermoelectric power (Seebeck effect), and magnetoresistance. In addition, electronic band-structure calculations were performed. We established that at ambient conditions the golden polymorph of Ti_2O_3 behaves as a semiconductor with an energy gap of ∼0.1–0.2 eV and determined its typical electronic band structure parameters.

DOI: 10.1103/PhysRevB.86.024106 PACS number(s): 62.50.−p, 72.20.My, 72.20.Pa, 71.30.+h

I. INTRODUCTION

Sesquioxides, M_2O_3 (M is a metal or combination of metals), are the focus of interest of several fields, such as condensed matter physics, chemistry, geosciences, and others. Ambient polymorphs of binary sesquioxides demonstrate structural uniformity (Fig. 1), with a tendency to two symmetric lattices, one of the corundum-type (space group #167 $-R\bar{3}c$) for low periodic numbers Z of the cation and another one of the cubic-bixbyite-type (space group #206 $-Ia\bar{3}$) for high Z. This class of materials has enormous industrial potential. Its representatives, such as numerous manganites, titanates, ferrites, and others, are widely utilized in various technologies.

High-pressure high-temperature (HP-HT) studies of these systems found that their ambient phases are stabile in limited pressure-temperature ranges. Binary corundum-structured sesquioxides (e.g., Al_2O_3, α-Fe_2O_3, Cr_2O_3) under pressure exhibit transitions, first to a Rh_2O_3 (II)-type lattice (space group #60 $-Pbna$) and then to a postperovskite lattice (supposedly of the $CaIrO_3$-type, space group #63 $-Cmcm$).[1–4] Recently, a new high-pressure polymorph with the U_2S_3- or Th_2S_3-type structure was proposed to appear in these systems.[5] It was predicted to be stabile in Al_2O_3 above 370 GPa[5] and found experimentally in Ti_2O_3 treated at 15–20 GPa and 1000–2000 °C.[6,7] Some of cubic-bixbyite-structured oxides (e.g., In_2O_3[8]) under pressure transform to the corundum and Rh_2O_3 (II)-type lattices, suggesting a transformation scenario similar to the one in the corundum-structured systems.[1–4] However, higher pressure studies on several of them, namely Sc_2O_3, Y_2O_3, and In_2O_3, established that they ultimately transform to another lattice with the α-Gd_2S_3-type (space group #62 $-Pnma$).[9–11]

The HP-HT polymorph of Ti_2O_3 with the Th_2S_3 structure was found to be fully recoverable and stabile at ambient conditions.[6,7] Contrary to other oxides, it has a puzzling golden color.[7] The Th_2S_3- or U_2S_3-type structures are common only for sulfides, selenides, and tellurides, and hence, properties of the oxide adopting this phase may be unusual. Thus, the golden polymorph of Ti_2O_3 with the Th_2S_3 structure is a good example to investigate properties of strongly compressed sesquioxides. In addition, a better understanding of both HP-HT conditions of synthesis of this polymorph and its properties could help in designing of HP-HT routes toward new tatanate oxides, (M,Ti)O_3 with emergent properties.

In the present work we examine the P-T diagram of Ti_2O_3 and establish conditions of its transformation to the golden phase. We perform detailed experimental investigations of structural, optical, and transport properties of the golden of Ti_2O_3 and supplement it by electronic band structure calculations. We figure out typical parameters of the electronic band structure of the golden phase.

II. DETAILS OF EXPERIMENT AND THEORY

A. HP-HT synthesis

As it follows from the previous studies[6,7] the golden Th_2S_3-type phase of Ti_2O_3 may be routed by means of HP-HT synthesis. Microscopic amounts of Th_2S_3-structured samples may be simply obtained in conventional diamond anvil cells under compression of a corundum-structured sample and consequent heating by means of an external heater or internal heating by a high-power laser beam. Bulk ingots may be prepared in large-volume presses under multitonne pressures.

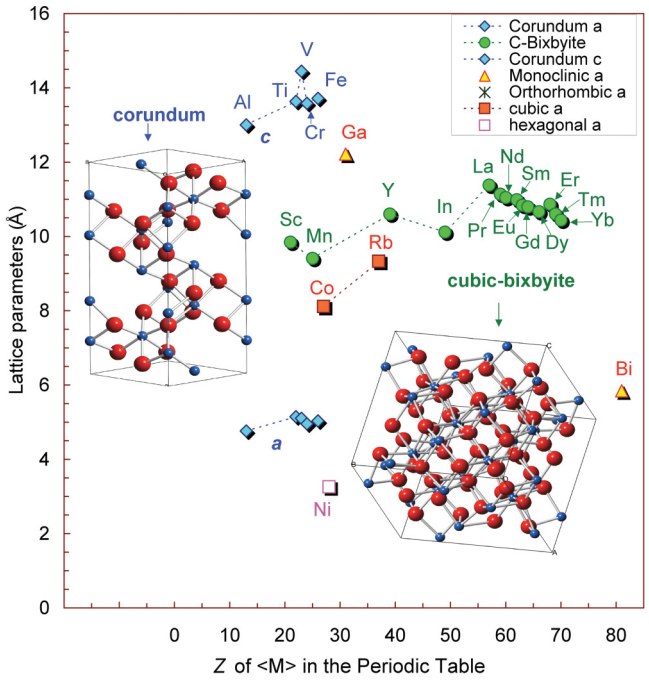

FIG. 1. (Color online) Lattice parameters vs atomic numbers (Z) of cations in selected sesquioxides, M_2O_3 (M is a metal). The plot clearly shows two trends: corundum structure for low Z and cubic bixbyite structure for high Z. The unit cells of these two structures are shown on the plot.

In the present work we employed both methods. For starting material we used commercial fine corundum-structured Ti_2O_3 powder of 99.8% purity from Alfa Aesar.

The synthesis of golden Th_2S_3-structured Ti_2O_3 in diamond anvil cells was combined with high-pressure investigations of structural and optical properties of the conventional corundum phase of Ti_2O_3. We employed a cell with culet of 400 μm and a rhenium gasket with a drilled hole filled with a LiF pressure-transmitting medium, providing a sufficient quasihydrostaticity in the range up to 15–20 GPa.[12] The pressure gradient near the sample was controlled by measurements of the shift of the luminescence line of several ruby balls situated around the sample. Each pressure value was obtained by averaging the pressure values of the ruby chips. The average pressure inside the cell was further determined using data of the equation of state of LiF.[12,13] The difference between both values did not exceed 0.5–1 GPa up to the maximal pressure, 18.6 GPa. Using LiF as a calibration material the distance between the sample and the detector was accurately determined at each pressure point. This approach allowed improving the accuracy in the determination of the lattice parameters of Ti_2O_3 as a function of pressure.

Bulk polycrystalline ingots of golden Ti_2O_3 were obtained by use of 1200- and 5000-tonne multianvil presses at Bayerisches Geoinstitut (BGI). The samples were pressurized in cylindrical capsules made out of 25-μm-thin rhenium foil that protected them from contamination and chemical reactions with surroundings. A capsule was embedded into a double cylinder, the external layer of which was made out of $LaCrO_3$, was employed as a heater and was insulated from the capsule by an internal MgO layer. The temperature of the synthesis was determined by means of W3Re/W25Re thermocouples attached to one end of the capsule. The assembly was adjusted into an octahedral container made out of $(MgO)_{0.95}(Cr_2O_3)_{0.05}$. Pressure was generated between eight tungsten-carbide cubic anvils with truncated corners. The pressures were determined by calibration curves. A pyrophyllite gasket was employed as a pressure-transmitting medium.[14,15] Several samples of golden Ti_2O_3 have been synthesized. Their homogeneity and chemical composition was verified by means of both scanning electron microscope (SEM) studies by use of a LEO-1530 microscope and of a microprobe analysis at JEOL JXA-8200 electron microscope. Most physical property measurements were done on two samples, labeled A (17 GPa, 1000 °C, 2 hours) and B (22 GPa, 1800 °C, 3 hours).

B. Measurements of structural and optical properties at ambient and high pressures

All samples prepared by HP-HT treatment were characterized by x-ray diffraction (XRD) and Raman studies. Ambient and high-pressure XRD studies were performed using a Rigaku diffractometer (wavelength 0.7108 Å). High-quality ambient XRD studies were performed at the Swiss-Norwegian Beam Lines (SNBL), Grenoble, France with a wavelength of 0.7015 Å. Raman spectra both at ambient and high pressures were excited with the red 632.8-nm line of a He-Ne laser and were recorded using a LabRam spectrometer in a backscattering geometry.[15] A couple of samples were examined by reflectance and absorption spectroscopy on a Bruker IFS 120 Fourier-transform spectrometer coupled to an all-reflecting Bruker microscope. The samples were polished from both sides to a thickness of about 14–19 μm. The absorption/reflectance spectra were measured by use of a tungsten source, an Si-coated CaF_2 beam splitter, and a narrowband mercury-cadmium-telluride (MCT) detector. The spectra were measured in mid- and near-infrared and in visible ranges. Each spectrum was obtained by averaging over two spectra, each consisting of 200 scans. The spot size on the sample was varied from 30 to 200 μm to make sure of the absence of noticeable edge effects.

C. Measurements of transport properties

At ambient pressure, the electrical and galvanomagnetic properties of the samples were measured by a conventional Montgomery method (a modification of the Van der Pauw method) using an Oxford Instruments setup.[16] The measurements were performed at temperatures from 1.4 to 375 K. The galvanomagnetic investigations were carried out in magnetic fields up to 13.6 T. The ambient-temperature thermoelectric power was measured by a conventional method, i.e., a temperature difference, ΔT, was applied between two edges of a thermally isolated sample and the resulting thermoelectric voltage, U, was measured between these edges.[17] Then, a thermopower value was found as a linear coefficient between U and ΔT. Electrical resistivity, magnetoresistance (MR), and Hall effects were measured on bulk ingots, and the thermopower studies were performed on microscopic plates of ~300 μm in the diameter and ~30 μm in the thickness, cut from samples A and B.

D. Calculation of crystal and electronic band structures

Six candidate structures of Ti_2O_3 were designed, namely, corundum, Rh_2O_3(II)-type, perovskite, postperovskite, Th_2S_3-type, and α-Gd_2S_3-type, respectively. Theoretical simulations performed here were based on the density functional theory (DFT) with the generalized gradient approximation (GGA), as implemented in the VASP code.[18] We used the PAW-PBE potentials supplied with the VASP code and set the kinetic energy cut-off at 700 eV. For the Brillouin zone sampling, we used the Monkhorst-Pack scheme. The k-point meshes were $4 \times 4 \times 4$ for corundum-type and Rh_2O_3(II)-type Ti_2O_3; $6 \times 6 \times 4$ for perovskite-type Ti_2O_3; $6 \times 2 \times 4$ for postperovskite-type Ti_2O_3; $4 \times 4 \times 6$ for Th_2S_3-type Ti_2O_3; and $4 \times 4 \times 2$ for α-Gd_2S_3-type Ti_2O_3. For each crystalline phase, we obtained the minimum total energy in a constant volume by means of allowing the atoms and cell geometry to relax into their lowest energy configuration with a tolerance value taken as 10^{-4} eV per cell in the self-consistency cycles. The energy-volume data were then fitted by a third-order Birch-Murnaghan equation of state.[19] At the equilibrium volume of the Th_2S_3-type phase, we calculated the electronic band structure and density of states. We treated effects of exchange and correlation by GGA.[20] Efficiency of this approach was verified by a theoretical reproduction of the known scenario of the pressure-driven phase transition in TiO_2.[21]

III. RESULTS AND DISCUSSION

This section is divided into two parts. The first part (A) is devoted to the synthesis of the golden phase of Ti_2O_3. It considers both transformation ways from the corundum phase of Ti_2O_3 into the golden phase and a P-T phase diagram of Ti_2O_3. The second part (B) presents experimental results of structural, optical, and transport investigations of the golden phase of Ti_2O_3 and calculations of its electronic band structure.

A. Synthesis of the golden Th_2S_3-structured phase of Ti_2O_3

We performed more than a dozen experiments at HP-HT conditions, one in a high-pressure diamond anvil cell for *in situ* observation of the transition to the golden phase and others in multianvil cubic high-pressure cells for *ex-situ* studies of the golden phase (it was found to be perfectly quenchable to ambient conditions).[6,7]

1. Structural and optical properties of corundum-structured Ti_2O_3 under pressure; corundum → distorted corundum → golden phase transitions

In the first run the fine-powdered corundum-structured Ti_2O_3 was gradually compressed up to 18.6 GPa a diamond anvil cell with a LiF pressure-transmitting medium. X-ray diffraction patterns and Raman spectra (Figs. 2 and 3) were measured on the same sample. At the maximum pressure, the sample was laser heated for 20 minutes to temperatures above 2200 K and then slowly decompressed to ambient pressure.

Figure 2(a) shows the XRD patterns of Ti_2O_3 for the pressurization and decompression cycles. The stronger pressure evolution of the positions of the XRD reflexes of LiF [masked with shadow lines at Fig. 2(a)] reflects its softness in comparison with Ti_2O_3. The pressure dependences of the lattice parameters determined from these data are shown in Fig. 2(b). Above about 8 GPa, one can observe signatures of a structural distortion: gradual changes of both the lattice parameters with pressure result first to a dip in the c/a ratio and then to an appreciable growth above 12–13 GPa [Fig. 2(b)]. It was robustly established that at ambient pressure under moderate heating to above ~430 K, Ti_2O_3 undergoes a semiconductor-semimetal transition[22–25] at which the c/a ratio in the corundum structure jumps from ~2.65 to ~2.70, and then it saturates.[26–28] Consequently, in measurements of the electrical resistivity it was found that applied pressure both decreases the transition temperature and smoothes the transition itself.[29] Thus, at the maximal pressure of 1 GPa achieved in Ref. 29, the transition was seen near 370 K.[29] Therefore, the anomalies in the pressure dependence of the lattice parameters we observe around 8–12 GPa and, in particular, the growth in the c/a ratio [Fig. 2(b)], could be signatures of this transition. The abrupt rising in the c/a ratio with pressure to 18.6 GPa indicates that the transition is not completed even up to this maximal pressure.

The volumetric changes across the corundum → distorted corundum transition are shown in Fig. 2(c). The beginning of the transition may correspond to the curvature inversion point at the $V(P)$ curve [inset of Fig. 2(c)]. A pressure-driven lowering of the bulk modulus, B_0, of a material is a very rare and always a questionable phenomenon. Therefore, such an enhanced contraction of Ti_2O_3 beyond about 10 GPa may be addressed to a smoothed volume drop at a (quasi-)isostructural transition. As the transition is not completed up to 18.6 GPa, it is hardly possible to figure out this volumetric drop, while rough estimates suggest only $\Delta V \approx -1.5\%$ at 18.6 GPa. A strong scattering of the data for the corundum structure [Fig. 2(c)] does not permit us to precisely determine the bulk modulus. Our data show a higher B_0 than the one (B_0 = 206 GPa) reported in Ref. 6 [Fig. 2(c)] but correspond better to the theoretical value of $B_0 = 237$ GPa from Ref. 7. At ambient conditions the volumes per formula unit (V_0/Z) of the corundum and the golden phases were found to be ~51.87 and ~45.29 Å^3, respectively, i.e., the latter structure is denser by ~12.7% [Fig. 2(c)]. The XRD data for the golden phase collected in a several different experimental runs with neon as pressure-transmitting medium permit us to precisely determine the bulk modulus of this phase. Fitting the third-order Birch-Murnaghan equation of state to the data we find $V_0 = 181.1$ Å^3, $B_0 = 259.3$ GPa (at $B_0' = 4$). These values are in reasonable agreement with the calculated values ($V_0 = 184.3$ Å^3, $B_0 = 251$ GPa),[7] while the bulk modulus is a bit lower as the one ($B_0 = 296$ GPa) estimated from a set of five points in Ref. 6.

The simultaneous Raman spectroscopy examination of Ti_2O_3 under pressure corroborates the previous findings of the XRD studies. The corundum structure is expected to show seven Raman active modes with the irreducible representations of $2A_{1g} + 5E_g$. At ambient pressure, the Raman spectra showed five distinct peaks at 235.5, 275.5, 303.5, 347, and 509 cm^{-1} (Fig. 3, Table I). The frequencies of the peaks agree with the five basic peaks in Raman spectra reported earlier.[30–32] Pressure application up to 7 GPa leads only to a conventional hardening of these phonon modes due to contraction in the Ti-O bond lengths (Fig. 3). The Grüneisen parameters of

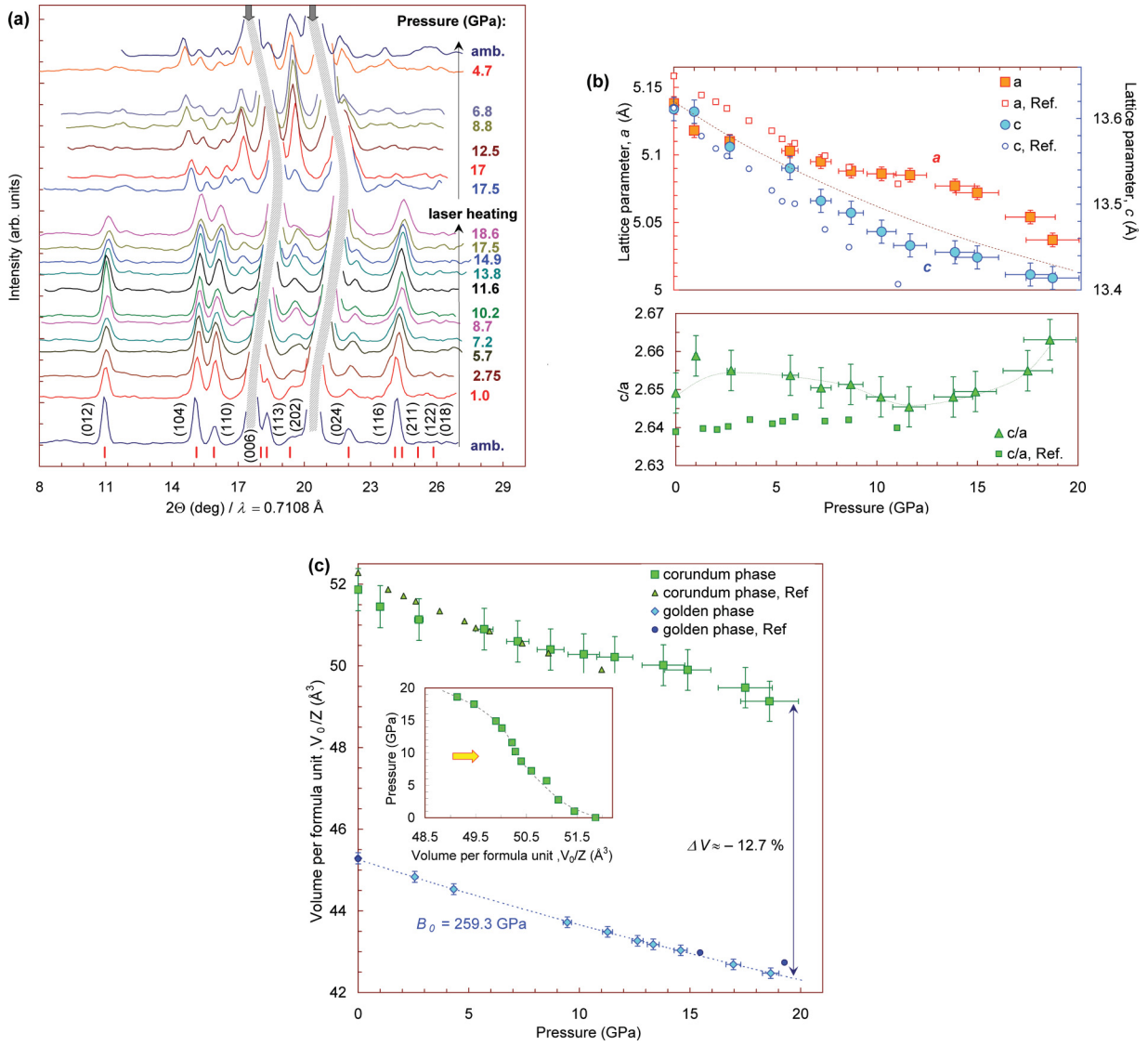

FIG. 2. (Color online) X-ray diffraction patterns (a) and unit-cell parameters (b) and (c) of Ti_2O_3 at ambient temperature under high pressure. (a) Selected XRD patterns of corundum-structured Ti_2O_3 under high pressures up to 18.6 GPa (pressure values are shown near the curves). They show a transformation to the golden phase after laser heating at 18.6 GPa, and conservation of this golden phase upon decompression to ambient pressure. The two hatched broad lines marked by the bulk arrows show evolution of the main reflexes of soft LiF powder. The *hkl* indexes of reflexes are given near the pattern taken at ambient pressure. (b) Pressure dependences of the lattice parameters a and c and its ratio c/a in the corundum structure of Ti_2O_3. Around 8–12 GPa one can notice anomalies at the curves that could suggest a structural distortion (Label Ref. denote data taken from Ref. 6). (c) Pressure dependencies of volume per formula unit (V_0/Z) for the corundum and the golden phases. Our curves for the corundum and the golden phases correspond to different runs (Label Ref. denote data taken from Ref. 6). Inset in (c) better shows volumetric anomalies across the corundum-distorted corundum transition under pressure of ~8–12 GPa. The bulk arrow indicates the inflection point of the $P(V)$ curve.

these modes are within a range of (1÷3) (Table I), which is typical for semiconductors. At 8.7 GPa the intensities of the main peaks at 235.5 and 275.5 cm^{-1} (at ambient pressure) diminish [Fig. 3(a)], and their phonon frequencies shift by ~20 and ~10 cm^{-1}, respectively [Fig. 3(b)]. This feature resembles those observed across the semiconductor-semimetal transition at ambient pressure: dips near 400–500 K in the temperature dependences of the frequencies.[31,32] Furthermore, the abnormal pressure dependence of the mode at 235.5 cm^{-1} across the transition is a mirror reflection of the temperature dependence of that observed at ambient pressure.[32] One can see that the intensities of the Raman spectra decrease with pressure and tend to zero to 18.6 GPa [Fig. 3(a)]. At the same time, XRD patterns taken up to 18.6 GPa do not show any signatures of amorphization or structural degradation [Fig. 2(a)]. These data are an evidence of either a gradual metallization or strong disordering at the short-range order having no effect at the long-range order examined by XRD. The distorted corundum phase obtained by heating at ambient pressure showed a strong Raman signal[31,32] in consistence with its semimetallic but not metallic character.[26]

Detailed investigation of the corundum-distorted corundum and its P-T boundary was beyond the scope of the present work. For these studies high-quality single-crystalline samples

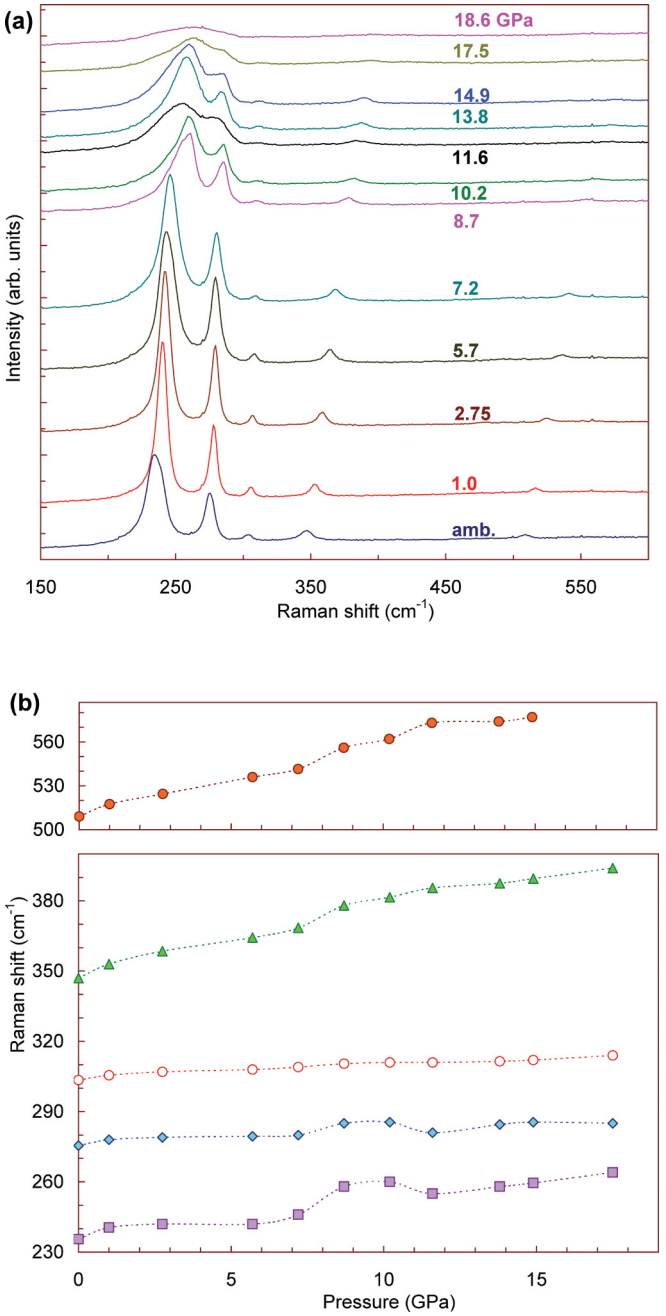

FIG. 3. (Color online) Raman spectra (a) and wave numbers (b) for corundum-structured Ti_2O_3 at ambient temperature under high pressure. (a) Selected Raman spectra of corundum-structured Ti_2O_3 under high pressures up to 18.6 GPa (pressure values are shown near the curves). (b) Pressure dependences of the phonon frequencies in the corundum structure of Ti_2O_3. Around 8–12 GPa one can notice the anomalies at the curves that corroborate the features at Fig. 2.

of Ti_2O_3 are more preferable, since Ti_2O_3 is known to be able to show both modification in its defect structure and stoichiometric deviations.[33] Furthermore, pressure value of the phase transition may be sensitive also to a pressure-transmitting medium.

After heating the sample above 2200 K at 18.6 GPa we registered new XRD lines suggesting a structural transition [Fig. 2(a)]. The positions of these XRD reflexes matched with those expected for the Th_2S_3-type phase. This phase remained stable under pressure releasing to ambient. Thus, the golden phase resulted from the heating of the distorted corundum one, and, hence the latter, to some extent, may be considered as an intermediate phase in the corundum → golden phase transition. It is interesting to note that Ti_2O_3-based systems (e.g., $FeTiO_3$ and $TiMnO_3$) recently revealed a tendency to decomposition under HP-HT conditions, near 40−50 GPa.[34–36] The lattice dynamics calculations suggest the stability of Ti_2O_3 against decomposition at least up to about ∼150 GPa.[7]

2. *HP-HT synthesis and P-T phase diagram of Ti_2O_3*

All samples synthesized at HP-HT conditions in multianvil cubic cells were *ex-situ* examined in XRD and Raman studies. An example of the Rietveld refinement of the golden phase is given in Fig. 4. Thus, the golden phase was confirmed to adopt the Th_2S_3-type structure (space group #62 $-Pnma$) with the unit-cell parameters as follows: $a = 7.8248(6)$ Å, $b = 2.8507(4)$ Å, $c = 8.0967(3)$ Å, $V = 180.61(1)$ Å^3, and $Z = 4$. The refined atomic coordinates are presented in Table II; these results agree with those reported earlier.[6] Figure 5 summarizes our experimental data (points labeled from A to I, and DA) and those from Refs. 6 and 29. Thus, a positive slope of roughly ∼500 K/GPa of the P-T boundary of the golden phase has been established (Fig. 5). The samples prepared at lower pressures (points G and H) adopted the conventional corundum structure (the distorted corundum phase is unquenchable as the transition is reversible) (Fig. 5).

The high-temperature region above 2400 K remains questionable. In a couple of runs carried out at 11.5 GPa and 2623 K (point F) and 15.5 GPa and 2573 K (point I) (Fig. 5), the samples were substantially and non-uniformly contaminated with the materials surrounding a sample's capsule. However, it is interesting to note that some pieces of the contaminated Ti_2O_3-rich alloys showed different XRD patterns that resemble, e.g., those of perovskite ($GdFeO_3$-type, $Pbnm = Pnma$ space group − #62) or Rh_2O_3(II)-type structures ($Pbna$ space group − #60). Thus, Ti_2O_3 may be a promising material for structural engineering: Under appropriate and controlled doping combined with a HP-HT synthesis one can stabilize different high-pressure structures. The results of lattice dynamics calculations strongly suggest that potential intermediate structures, i.e., major phases of sesquioxides, like perovskite, Rh_2O_3(II)-type, and postperovskite, are not stable in Ti_2O_3 [Fig. 4(b)]. However, since the corundum and the Th_2S_3-type phases are structurally mismatched and the transition mechanism is vague, one cannot absolutely exclude the *probable* existence of perovskitelike, postperovskitelike, or other intermediate structures in pure Ti_2O_3 as well. These potential phases may be metastable or may have a very narrow stability range [Fig. 4(b)], and for these reasons they could remain undiscovered in our studies.

The P-T diagram shows that there is no direct boundary between the original corundum and the Th_2S_3-type phases (Fig. 5): the minimal transition pressure to the Th_2S_3-type phase is close to 10 GPa, but near this pressure value at ambient temperature the corundum lattice starts to transform into the distorted corundum one (Figs. 2 and 3). This structural

TABLE I. Raman frequencies of corundum phase of Ti_2O_3 at ambient conditions. Pressure coefficients of these frequencies [Fig. 3(b)] and their Grüneisen parameters ($\gamma_i = \frac{B_0}{\omega_i}(\frac{\partial \omega_i}{\partial P})_{P=0}$, $B_0 = 237$ GPa was taken from Ref. 7) were calculated for 0–7 GPa range.

Peak, ω (cm^{-1})	ω' (cm^{-1} GPa^{-1})	ω'' (cm^{-1} GPa^{-2})	γ (Grüneisen parameter)	Raman peaks found in other studies		
				Ref. 30	Ref. 31	Ref. 32
235.5	1.94	−0.118	1.95	238	228	238
275.5	1.44	−0.129	1.24	279	269	279
303.5	1.36	−0.094	1.06	303	302	308
347	4.36	−0.221	2.98	347	347	350
				460	452	465
509	6.05	−0.243	2.82	508	530	513
				565	564	567

distortion with a possible displacement of the atoms could be a preparatory episode for the transition to the golden phase. Possible metallization in the distorted corundum phase near to 20 GPa indicates that the low-temperature region at these pressures (Fig. 5) potentially may show interesting physical properties. To date, an insulator-metal type transition was observed in other systems crystallizing in the corundum structure at ambient conditions, like Fe_2O_3 above ∼50 GPa,[37–39] V_2O_3 at ambient and high pressures,[40–44] and Cr_2O_3 at pressures above ∼50 GPa.[37] However, no signatures of superconductivity were so far observed.

It is interesting to compare the behavior of Ti_2O_3 with another member of the corundum family, namely V_2O_3, which exhibits a metal-insulator-type transition under temperature:[40–44] near 150 K the ambient corundum phase of V_2O_3 having a high electrical conductivity transforms into

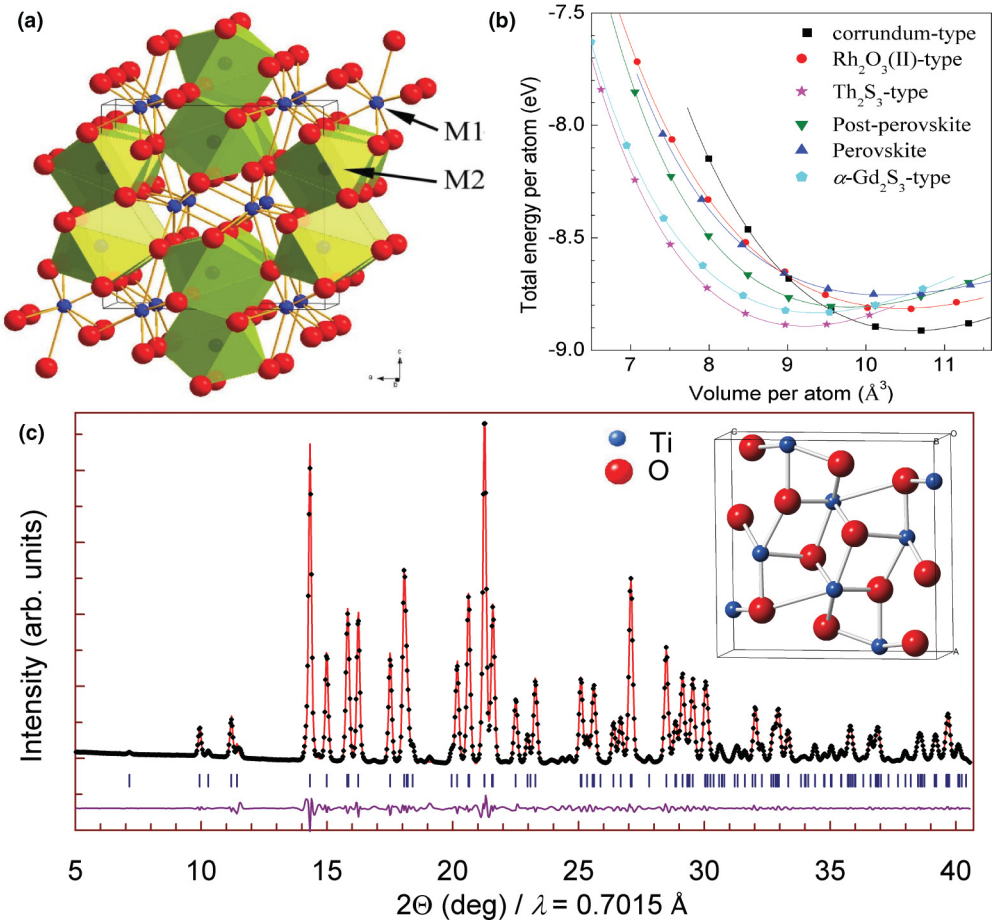

FIG. 4. (Color online) Crystal structure of the golden phase of Ti_2O_3. (a) General view of the crystal structure along the *b* axis. (b) Summarizes lattice energies of several possible structures in Ti_2O_3 and suggests the structural stability of the Th_2S_3-type lattice (data from Ref. 7). (c) Examples of Rietveld refinement of x-ray diffraction pattern of the golden phase of Ti_2O_3 taken at ambient conditions. Points are experimental data, solid lines are calculated profile, dashes denote expected reflex positions for the Th_2S_3-type phase, and the lowermost curve gives the difference between the experimental and the calculated profiles. Inset in (c) shows unit cell of the Th_2S_3-type phase.

TABLE II. Parameters of the unit cell of the golden phase of Ti_2O_3 at ambient pressure (Fig. 4).

Unit cell:	space group #62 – *Pnma*, structural type – Th_2S_3, lattice parameters: $a = 7.8248(6)$ Å, $b = 2.8507(4)$ Å, and $c = 8.0967(3)$ Å, $V = 180.61(1)$ Å^3, $Z = 4$				
Atomic coordinates:	x		y	z	
Ti_1	0.0279		$^1/_4$	0.3165	
Ti_2	0.1952		$^1/_4$	0.9822	
O_1	0.9432		$^1/_4$	0.8704	
O_2	0.1237		$^1/_4$	0.5545	
O_3	0.7901		$^1/_4$	0.1885	
Ti_1-O distances (in Å)			Ti_2-O distances (in Å)		
Ti_1-O_1	2.0911	× 2	Ti_2-O_1	2.1697	
Ti_1-O_2	2.0677		Ti_2-O_1	2.1515	× 2
Ti_1-O_2	2.1283	× 2	Ti_2-O_2	2.0934	× 2
Ti_1-O_3	2.0521		Ti_2-O_3	2.7677	
Ti_1-O_3	2.1299		Ti_2-O_3	1.9887	× 2
⟨Ti_1-O⟩	2.098		⟨Ti_2-O⟩	2.176	

a low-temperature monoclinic phase with a low electrical conductivity.[40–44] The transition in V_2O_3 is clearly of the Mott type. In Ti_2O_3 the correlation effects appear to be much weaker than those in V_2O_3,[45] but theoretical investigations still find that they should play a significant role in the transition.[46] The transition temperature in V_2O_3 also gradually decreases with applied pressure, and at near 3 GPa it abruptly falls down to 0 K.[41,42] Thus, the boundary of this metal-insulator-type transition in V_2O_3[42,43] qualitatively resembles the proposed

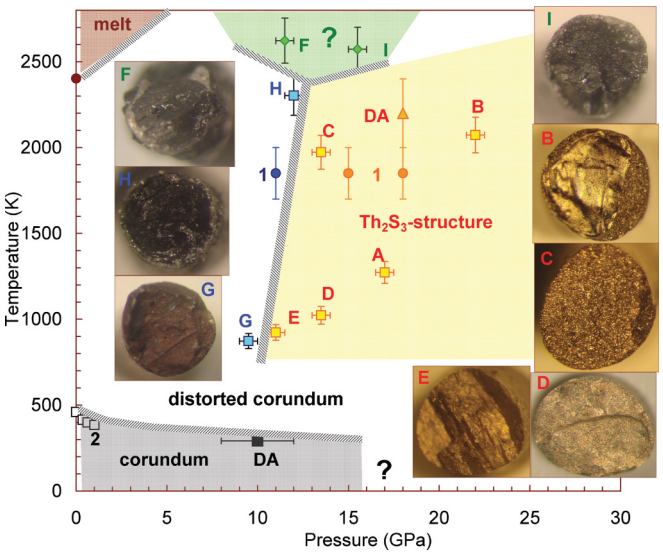

FIG. 5. (Color online) Pressure-temperature phase diagram of Ti_2O_3. Points labeled as *A*–*I* are results of HP-HT syntheses of bulk samples in multianvil cells, and points marked by *DA* are obtained by synthesis in diamond anvil cells; 1, data from Ref. 6; 2, data from Ref. 29. The golden phase is stable at least up to 74 GPa (Ref. 7). Photos of selected samples are given at the plot. Two question marks in the diagram indicate two not yet clarified regions in which some other structural or electronic phases potentially could exist: at high temperatures above 2500 K and at helium/nitrogen temperatures in the distorted corundum phase with possible metallic conductivity near above 15 GPa.

boundary between the corundum (low conductive) and distorted corundum (high conductive) phases in Ti_2O_3 (Fig. 5). Very recently, it has been demonstrated that the metal phases of V_2O_3 that have been obtained by heating the insulating phase on the one hand, and by pressure application to the insulating phase at low temperature on the other hand, are not equivalent and are characterized by essentially different properties.[47] It looks as though the border of the golden phase separates the stability region of the distorted corundum phase near about 10 GPa (Fig. 5), and hence, a similar situation may take place in Ti_2O_3 too. Thus, Ti_2O_3 gives an opportunity to investigate a *P*-*T* diagram of a transition metal oxide across the insulator-metal-type transition. At the moment, the behavior of such systems was studied based on the example of V_2O_3.[44]

B. Physical properties of the golden phase of Ti_2O_3

1. Structural and optical properties

All samples synthesized at HP-HT conditions were examined by both XRD and Raman spectroscopy studies. All samples adopting the Th_2S_3-type structure show a perfect reproducibility of XRD patterns and Raman spectra. A few samples were examined by high-resolution XRD studies using synchrotron radiation at the European Synchrotron Radiation Facility (ESRF); no difference between the samples was found. The perfect quality and consistency of the Raman spectra of the samples adopting the Th_2S_3-type structure suggests that the samples have no disordering at the short-range order. The Raman spectra of the golden phase of Ti_2O_3 have been already presented and discussed in Ref. 7. Scrupulous analysis of the Raman spectra measured on several samples, labeled as *A*-*E* (Fig. 6), shows that the only apparent trend is a shift of the phonon frequencies as function of the treatment temperature (insets in Fig. 6). This feature is robust because (i) the effect was reproducible when measured at different points of the samples, (ii) performance of the spectrometer was periodically controlled by checking the main Raman peak of Si near 520 cm^{-1}, and (iii) spikes of the plasma lines of the laser that sometimes appear in the spectra evidence a shift

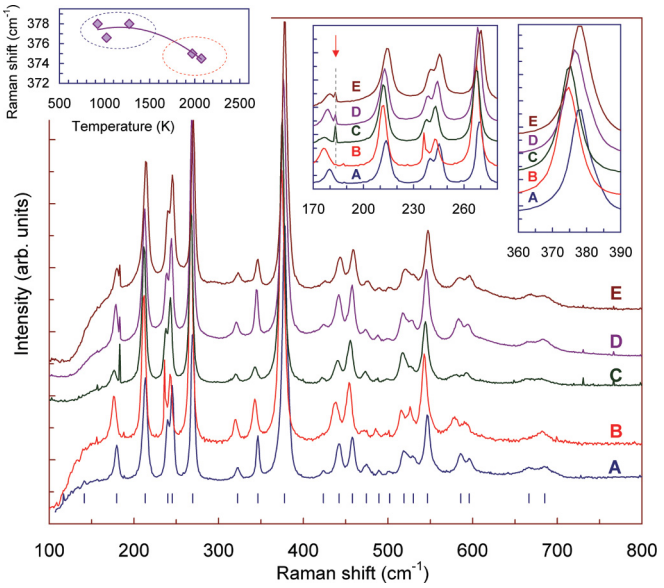

FIG. 6. (Color online) Raman spectra of the golden phase of Ti_2O_3 measured at ambient conditions on several samples, labeled *A*–*E* (from Fig. 5). Dashes below spectrum for sample *A* indicate peaks positions for this sample. Two right insets show low-frequency regions in enlarged scale between 170 and 280 cm^{-1} and around the main peak at ∼375 cm^{-1}. Dashed line and arrow at the inset show the position of one of the plasma lines. The left inset shows the position of the main peak as function of HP-HT synthesis temperature.

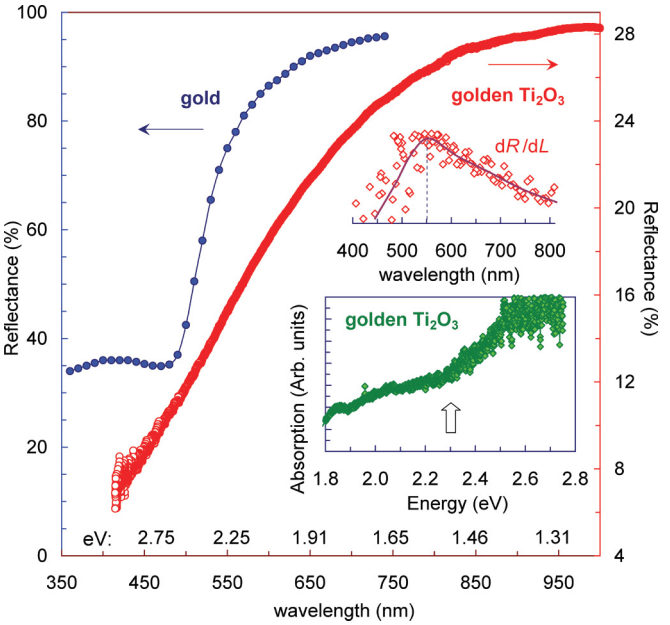

FIG. 7. (Color online) Reflectance spectra of the golden phase of Ti_2O_3 measured on sample *A* (right scale). Wavelength energies are also shown near the *x* axis. For comparison a spectrum of elemental gold metal (Au) is given from Ref. 49 (left scale). Both spectra show significant growth in reflectance above ∼500 nm. This can explain the golden color of gold and Th_2S_3-type Ti_2O_3. Upper inset shows the first derivative of reflectance, dR/dL; it has a maximum near 550 nm suggesting absorption edge of about 2.25 eV. Lower inset shows part of absorption spectra. Here one can see a growth in absorption coefficient above 2.3 eV (∼540 nm) (pointed by bulk arrow).

in the phonon frequency by 2–3 cm^{-1}. This small shift in the phonon frequencies could be related to a variation in the residual strains in the samples as well as to a strong variation in their mesostructure. Thus, HP-HT synthesis at temperatures below 1300 K gave submicrocrystalline samples with smooth surfaces of dark gold color (samples *D* and *E* in Fig. 5), while the samples prepared above 2000 K contained much larger crystallites (of up to several μm in diameter), and they have less smooth and more shiny golden surfaces (samples *B* and *C* in Fig. 5).

In order to probe the electronic band structure of the golden phase, we carried out combined mid- and near-infrared absorption spectroscopy studies on selected double-sided polished samples. These studies find that the golden phase is not transparent for energies above 0.1 eV. However, because of instrumental limitations the spectra could not be measured at energies below 0.1 eV, and, hence, we cannot exclude the existence of absorption edge below 0.1 eV. It should be stressed that the measurements were performed on the available microcrystalline samples. Often the sample's quality and, in particular, voids between grains, is crucial in these studies. Even in high-quality single crystals an intrinsic absorption edge may be strongly smoothened or even hidden by contributions related to defects, electron-hole, and other interactions.[48] Therefore, based on these data we cannot figure out any robust conclusion regarding the type of electronic band structure of the golden phase of Ti_2O_3. We clarify this issue further by transport methods and band structure calculations.

Apparently, the nontransparent golden Ti_2O_3 has no optical band gap in the visible spectral range. However, the reflected golden color hints that the Th_2S_3-structured Ti_2O_3 might have some features in a range of 400-1000 nm. Therefore, we examined its reflectance/absorption in a range of 400–1000 nm (Fig. 7). We find that the reflectance of a well-polished surface of the golden Ti_2O_3 dramatically changes with wavelength with a smooth crossover around 450–700 nm (Fig. 7). The first derivative of the reflectance, dR/dL, exhibits a flat maximum near 550 nm (upper inset in Fig. 7). This corresponds to the absorption edge of 2.25 eV. A direct investigation of optical absorption finds evidence of a smooth growth in absorption coefficient above 2.3 eV (lower inset in Fig. 7). Thus, the golden polymorph of Ti_2O_3 absorbs radiation with wavelength less than 540 nm and noticeably reflects the radiation with the higher wavelengths. This explains the golden color of Ti_2O_3 with the Th_2S_3-type structure as well as minor fluctuations in the color from sample to sample. We can point out a correspondence of the cases of golden Ti_2O_3 and the noble metal-gold (Au).[49] Gold (Au) metal exhibits a dramatic change in its reflectance between 500–600 nm (Fig. 7)[49] as a sequence of a direct electronic transition from the *d* band to the *s* one that crosses the Fermi level.[49] An absorption edge of gold was found at energies of ∼2.3–2.4 eV,[49] i.e., similar to that in the golden Ti_2O_3. Comparing the reflectance spectra of metal gold and golden Ti_2O_3 (Fig. 7), one can figure out that the latter may not be metallic since its reflectivity is much lower and would correspond to a semiconductor case.

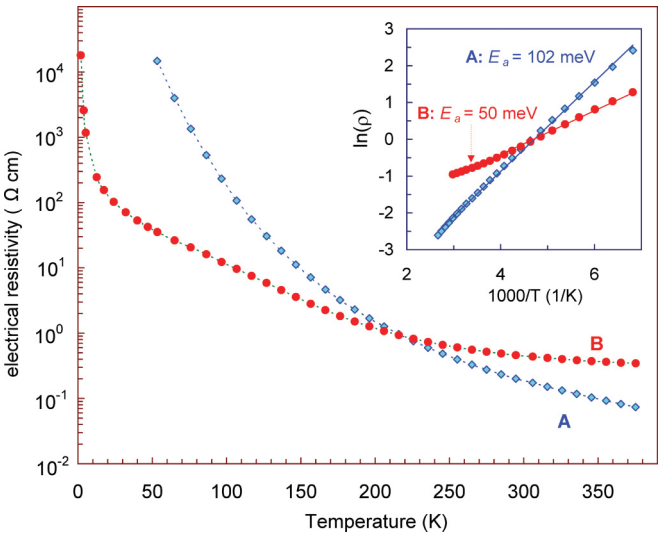

FIG. 8. (Color online) Temperature dependences of electrical resistivity, ρ, of the golden phase of Ti_2O_3. Labels *A* and *B* correspond to samples presented in Fig. 5. Inset shows $\ln(\rho)$ vs $1/T$ dependencies that strongly suggest activated character of electrical conductivity in 150–380 K range.

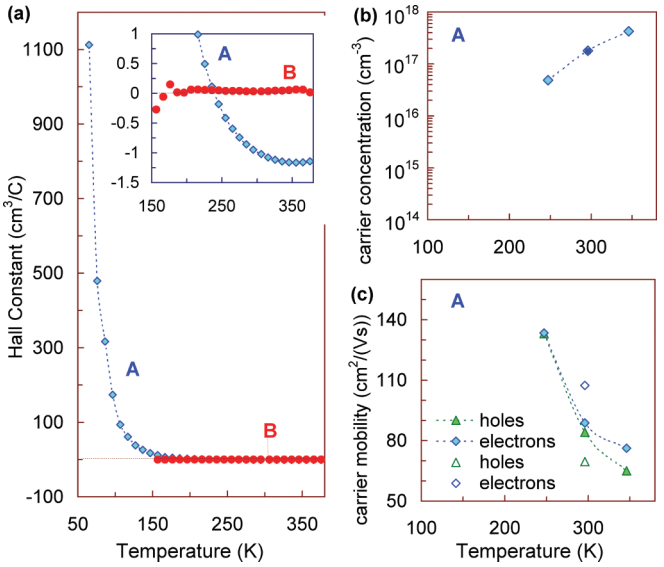

FIG. 9. (Color online) (a) Temperature dependences of Hall constants in the golden phase of Ti_2O_3 for samples *A* and *B*; inset shows region near zero Hall constant in enlarged scale. (b) and (c) Carrier concentration and mobility values estimated from two systems from Eqs. (1), (3), and (4) (filled symbols) and Eqs. (1), (4), and (5) (open symbols).

2. *Transport properties*

We measured electrical resistivity, Hall effect, MR, and thermoelectric power of samples *A* and *B* of the Th_2S_3-type Ti_2O_3 (Fig. 5). Based on these results we conclude that the basic type of the electronic band structure of the golden phase is most likely a narrow-gap semiconductor.

a. Electrical resistivity and Hall effect: one- and two-band conductivity models. The electrical resistivity of samples *A* and *B* of the Th_2S_3-type phase shows a semiconducting-like behavior for the whole temperature range investigated (Fig. 8). Thus, we rule out both metallic and insulating natures of the electrical conductivity in the golden phase, leaving options for the Th_2S_3-type phase to be a semiconductor or to be a semimetal. This issue can be resolved from a system of temperature dependencies of the electrical resistivity and Hall effect [Figs. 8 and 9(a)]. The Hall constant measured at 13.6 T shows a sign inversion near 200–250 K [Fig. 9(a)], and hence both electron and hole contributions are important for the electrical conductivity.

Normally, members of the titanium oxide family show temperature-dependent competition between electron and hole contributions into electrical conductivity.[50,51] In case of two-band conductivity, the electrical conductivity σ is given by[52]

$$\sigma = \frac{1}{\rho} = |e|(p\mu_p + n\mu_n), \tag{1}$$

where ρ is the electrical resistivity, e is the electron charge, p and n are the concentrations of holes and electrons, respectively and μ_p and μ_n are their mobility. In microcrystalline semiconductors and in general in systems with numerous defects, the electrical conductivity may be activated by both carrier transfers over band gap and by activation of carrier mobility [Eq. (1)]. The latter mechanism explains activation dependencies of electrical conductivity in semimetals and poor metals,[16,53] while it does not bring significant contribution for semiconductors.

In frames of a simple one-band model one can assume that in sample *A* the hole conductivity is dominating below 240 K (i.e., $\mu_p \gg \mu_n$), likewise, the electron conductivity above 240 K ($\mu_p \ll \mu_n$) (Fig. 9). Then, for these two limiting cases, the Hall carrier concentration n and mobility values μ may be estimated from the conventional well-known one-band expressions,[52] such as $n = 1/(eR_H)$ and $\mu_H = R_H/\rho$, where R_H is the Hall constant, and a Hall-factor is assumed to be equal to 1. We estimated $p \sim 5.6 \times 10^{15}$ cm^{-3} and $\mu_p \sim 0.28$ cm^2/(Vs) at 65 K, and $n \sim 6.6 \times 10^{18}$ cm^{-3} and $\mu_n \sim 4.7$ cm^2/(Vs) at 295 K. These carrier concentrations are reasonable for semiconductors but too low for semimetals. In addition, these two sets of carrier concentrations and mobility at 65 K and 295 K qualitatively indicate that the electrical conductivity is mainly governed by the carrier concentration rather than carrier mobility. Thus, these data [Figs. 8 and 9(a)] much better correspond to a semiconducting conductivity with conventional activation of charge carrier over a band gap.

The electrical resistivity of sample *A* rises rapidly with decreasing temperature and leaves our measurement range below 60 K (Fig. 8). This is a typical dependence for pure semiconductors with dominating intrinsic temperature-activated conductivity.[52] The electrical resistance of sample *B* becomes immeasurably high below 15 K (Fig. 8). Furthermore, the conductivity clearly shows an activation character (inset in Fig. 8). Neglecting the mobility contribution to activation of electrical resistivity (see the previous one-band estimations), one can roughly determine activation energies for samples *A* and *B* from the well-known expression as follows:[52]

$$\rho = \frac{1}{\sigma} = \rho_0 \exp\left(\frac{E_a}{kT}\right). \tag{2}$$

where ρ_0 is the constant, E_a is the activation energy, k is the Boltzmann's constant, and T is the temperature. Thus, from the temperature dependencies of electrical resistivity from 150 to 380 K the activation energies are found as $E_a = 0.102$ eV and 0.050 eV, respectively, for samples A and B (inset in Fig. 8). Hence, the energy gaps ($E_g = 2E_a$) for samples A and B are ~0.2 eV and ~0.1 eV, respectively. Notice that conventional corundum-structured Ti_2O_3 is also semiconducting with a similar energy gap of $E_g \sim 0.1 - 0.2$ eV.[54,55] The ambient-temperature values of electrical resistivity, 0.2 (0.46) $\Omega \times$ cm for sample $A(B)$ (Fig. 8) are consistent with the previous estimated energy gaps. Activation energies for semimetals with temperature-activated mobility are typically less than $\sim kT$ (e.g., $E_a = 14$ meV in single-crystalline Fe_3O_4[16]), and hence the above values are too high for semimetals.

Notice that at ambient conditions the μ_n/μ_p ratio in undoped p-type $R\bar{3}c$-Ti_2O_3 is ~0.5.[54] Therefore, for more accurate estimations of the band structure parameters in the Th_2S_3-type Ti_2O_3, a two-band conductivity model should be applied. Since the dominant conductivity is intrinsic (Fig. 8), potential extrinsic contributions should be minor and in a first approximation may be neglected. In a two-band model for weak magnetic field ($\mu B < 1$), the Hall Constant R_H comes as follows:[52]

$$R_H = \frac{r_H}{|e|}\frac{p\mu_p^2 - n\mu_n^2}{(p\mu_p + n\mu_n)^2}, \tag{3}$$

where r_H is the Hall's factor. Even though the electrical resistivity data (Fig. 8) suggest the dominant intrinsic conductivity (i.e., $p = n = n_i$), the number of variables (n_i, μ_p, μ_n) exceeds the number of equations [Eqs. (1) and (3)], and, hence, one needs more data for accurate determination of the aforementioned electronic band structure parameters.

b. Magnetoresistance. The MR effect is known to depend on carrier mobility; therefore, we measured that in sample A in magnetic fields, B up to 12 Tesla (Fig. 10). One can see that the MR effect is very small, less than 1% for the maximal magnetic field, 12 Tesla (Fig. 10). To improve an accuracy of these studies at each temperature point we measured the MR effect four times (for increasing and decreasing magnetic field of both polarities) and then averaged the data. Below ~247 K we could not obtain reliable data, since the effect was comparable with fluctuations in the signal. For ambient and elevated temperatures the MR effect is positive and squirelike ($\sim B^2$) for exception of a range of very low magnetic fields, at which the effect is zero or even slightly negative (Fig. 10). The MR effect obtained at 247.2 K is negative and looks like a function of $-aB^2/(1+cB^2)$, i.e., it is similar to quadratic in the low magnetic fields and tends to a saturation in high magnetic fields. This difference in the MR effects could be related to variations in carrier scattering mechanism at low temperatures.

In weak magnetic field the MR effect ($\Delta\rho/\rho$) comes as follows:[56]

$$\frac{\Delta\rho}{\rho} = B^2 b_r\left[\left(\frac{\sigma_n}{\sigma}\mu_n^2 + \frac{\sigma_p}{\sigma}\mu_p^2\right) - \left(\frac{\sigma_n}{\sigma}\mu_n - \frac{\sigma_p}{\sigma}\mu_p\right)^2 \times \frac{a_r^2}{b_r}\right], \tag{4}$$

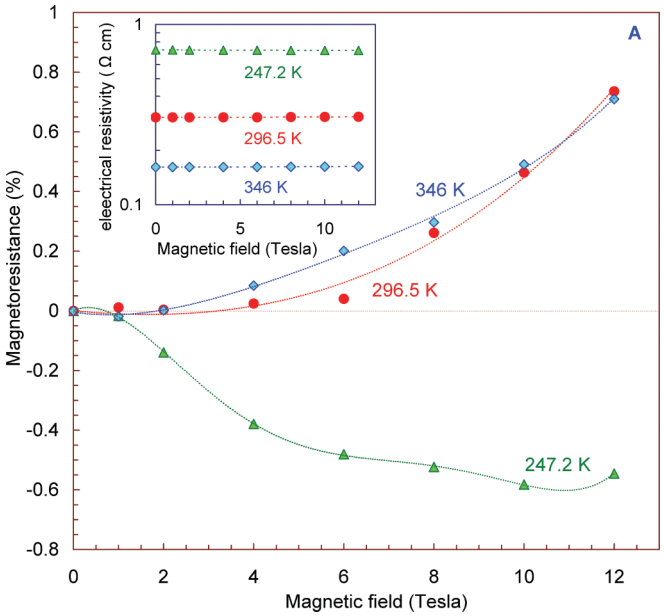

FIG. 10. (Color online) Magnetic-field dependences of magnetoresistance in sample A of the golden phase of Ti_2O_3 at several temperatures, given near the curves. Inset shows magnetic field dependences of absolute values of electrical resistivity for these temperatures.

where σ_n and σ_p are the electron and hole partial contributions to the total electrical conductivity, respectively; σ, a_r, and b_r are the constants, depending on scattering parameter r defining dependence of relaxation time τ on electron energy ε: $\tau(\varepsilon) \sim \varepsilon^r$. In case of intrinsic semiconductor conductivity ($p = n = n_i$), σ_n/σ and σ_p/σ are equal to $\mu_n/(\mu_n + \mu_p)$ and $\mu_p/(\mu_n + \mu_p)$, respectively [Eq. (1)]. Hence, Eqs. (1), (3), and (4) form a system that might be solved to determine values of n_i, μ_p, and μ_n for sample A. Since the values of a_r and b_r factors are also unknown, the MR effect in the case of two-band conductivity may be effectively considered by analogy with the simple one-band case as follows:[52,57] MR $\sim (\mu_{\text{eff}} B)^2$, where μ_{eff} is the effective mobility that accounts contributions from different bands; usually μ_{eff} is assumed to be a function as follows: $\mu_{\text{eff}} = \sqrt{\mu_n \mu_p}$.[52,57] Thus, fitting the MR effect at 296.5 K (346 K) (Fig. 10) by $A_1 \times (\mu_{\text{eff}} B)^2$ function we determine $A_1(\mu_{\text{eff}})^2 \approx 7.5\ (5.0) \times 10^{-5}$ m^4/(Vs)^2. The constant A_1 depends on the scattering mechanism of charge carriers and are determined by Fermi integrals.[52,56] For a typical case of acoustic phonon scattering (scattering parameter $r = -1/2$), $A_1 = 9\pi/16 \times (1 - \pi/4) \approx 0.38$.[52,56] This A_1 constant, like the Hall's factor, r_H, is of order of 1 and hence may be omitted. Disregarding this A_1 constant (i.e., assuming $A_1 \sim 1$ for 296.5 K and 346 K, and $A_1 \sim -1$ for 247.2 K) one can qualitatively estimate effective mobility values from the MR effect. Thus, at 247.2, 296.5, and 346 K, μ_{eff} equals to ~133, 86, and 70 cm^2/(Vs), respectively. For $B < 5$ Tesla, the absolute magnitude of MR effect at 247.2 K is much larger than those at 296.5 and 346 K (Fig. 10). This is visual evidence of mobility growth with temperature lowering; this indicates the inconsistence of the one-band approaches that would lead to the opposite result (see previous paragraph, a).

This is the evidence against semimetallic conductivity with temperature-activated mobility, e.g., the case of Fe_3O_4.[16]

Hence, the electrical resistivity (Fig. 8), the Hall effect [Fig. 9(a)], and the MR effect (Fig. 10) form a system (Eqs. (1) and (3) and $\mu_{\text{eff}} = \sqrt{\mu_n \mu_p}$) that could be solved with respect to n_i, μ_p, and μ_n. Meanwhile, it should be stressed that mobility values determined from the Hall and MR effects are often different since Hall mobility strongly depends on electrical barriers like dislocations and voids and is usually being underestimated;[16,52,56] for approximate estimation this difference may be ignored. We solved this system analytically for sample *A* at 247.2, 296.5, and 346 K, taking starting values of carrier mobility μ_p and μ_n very close to μ_{eff}. We obtained three sets of values as follows: (i) at 247.2 K, $n_i = 4.9 \times 10^{16}$ cm^{-3}, $\mu_p = 133.1$ $\text{cm}^2/(\text{Vs})$, and $\mu_n = 133.5$ $\text{cm}^2/(\text{Vs})$; (ii) at 296.5 K, $n_i = 1.8 \times 10^{17}$ cm^{-3}, $\mu_p = 84.1$ $\text{cm}^2/(\text{Vs})$, and $\mu_n = 88.8$ $\text{cm}^2/(\text{Vs})$; and (iii) at 346 K, $n_i = 4.3 \times 10^{17}$ cm^{-3}, $\mu_p = 65.1$ $\text{cm}^2/(\text{Vs})$, and $\mu_n = 76.3$ $\text{cm}^2/(\text{Vs})$ [Figs. 9(b) and 9(c)]. The temperature dependencies of these carrier concentration and mobility values [Figs. 9(b) and 9(c)] are typical for semiconductors. A rapid growth in the carrier mobility with temperature lowering [Fig. 9(c)] is characteristic for intrinsic semiconductor conductivity with phonon scattering mechanism of carriers ($\mu \sim T^{-3/2}$)[52,56] but not consistent with charged impurities scattering mechanism of carriers.

The case of sample *B* synthesized at higher temperature looks a bit different from sample *A* but might also be described in the same model of completion between the hole and electron partial conductivities. For instance, near-zero Hall constant for sample *B* in the range of 150–380 K [Fig. 9(a)] might suggest the equivalence of the electron and hole contributions (mobility values). However, other interpretations are also possible.

c. Thermoelectric power. To obtain independent information concerning the dominant type of conductivity (electrons or holes) in the golden phase of Ti_2O_3 at ambient conditions, we applied a thermoelectric power *S* technique. Contrary to other transport studies the thermopower studies were performed on microscopic plates (see the experimental section) that provided a new insight into the electronic transport. In all plates cut from sample *A* we registered the negative thermopower values of $S \sim -(80 \div 95)$ μV/K at room temperature. One example is shown in Fig. 11(a). The negative sign of the thermopower in sample *A* [Fig. 11(a)] agrees with the negative values of the Hall constant near ambient temperature [inset in Fig. 9(a)] and suggests *n*-type conductivity. The thermopower value is a result from a competition of electron and hole partial contributions (σ_n and σ_p, respectively) to the electrical conductivity, as follows:[52]

$$S = -\frac{k}{|e|}\left\{\frac{\sigma_n}{\sigma}\left(r_n + \frac{5}{2}\right) - \frac{\sigma_p}{\sigma}\left(r_p + \frac{5}{2}\right) + \frac{\sigma_n - \sigma_p}{\sigma}\frac{E_g}{2kT} - \frac{3}{4}\ln\frac{m_p}{m_n}\right\}, \quad (5)$$

where $m_n(m_p)$ and $r_n(r_p)$ are the effective mass and scattering parameter of electrons (holes), respectively. Since the effective masses of carriers (m^*) are related to their mobility ($\mu = |e|\tau/m^*$, where τ is the impulse relaxation time of carriers), the last term in Eq. (5) ($^3/_4(\ln(m_p/m_n))$) also depends on the μ_n/μ_p ratio (if we disregard the difference in τ for holes and electrons). Since the temperature dependence of

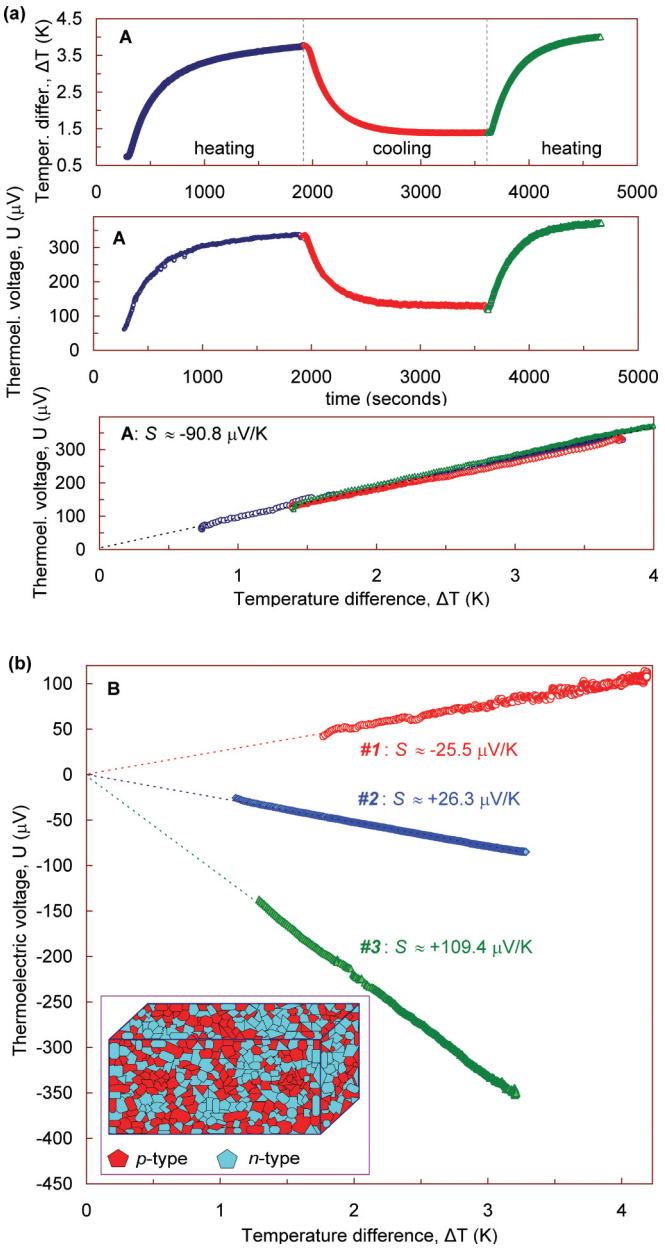

FIG. 11. (Color online) Ambient thermoelectric power (*S*) of the golden phase of Ti_2O_3 for samples *A* (a) and *B* (b). (a) Procedure of thermopower determination on example of sample *A*. Thermopower value was measured by conventional method: one applies temperature difference ΔT between two edges of a sample that is fully isolated from environment (a, upper plot) and measures thermoelectric voltage *U* that is induced by this ΔT (a, middle plot), between these edges; thermopower value is found as an inverted linear coefficient between *U* and ΔT (a, lower plot). This example shows a triple heating-cooling-heating cycle performed on automated setup (Ref. 17). In this case a thermopower value is determined by averaging of all the heating-cooling-heating cycles and is found to be equal to $S \approx -90.8$ μV/K. (b) Diversity of thermopower values in sample *B*: three pieces cut from sample *B* and labeled as #1–#3 exhibit different thermopower values. Proposed geometrical model of conductivity type in sample *B* is given as inset in (b).

TABLE III. Parameters of electronic band structure of the golden phase of Ti_2O_3 [on example of sample *A* (Fig. 5)].

Property	Comment or value
Electrical conductivity mechanism	Intrinsic two-band conductivity
Dominant type of electrical conductivity at 296 K	*n*-type
Estimations from Hall effect, MR, and resistivity	
Carrier concentration at 296 K (in cm^{-3})	1.79×10^{17}
Hole mobility at 296 K [in $cm^2/(Vs)$]	84.1
Electron mobility at 296 K [in $cm^2/(Vs)$]	88.8
Partial electron (hole) conductivity at 296 K, σ_n/σ (σ_p/σ)	0.514 (0.486)
Estimations from thermopower, MR, and resistivity	
Carrier concentration at 296 K (in cm^{-3})	1.75×10^{17}
Hole mobility at 296 K [in $cm^2/(Vs)$]	69.6
Electron mobility at 296 K [in $cm^2/(Vs)$]	107.4
Partial electron (hole) conductivity at 296 K, σ_n/σ (σ_p/σ)	0.607 (0.393)
Magnetoresistance effect at 296 K	Mostly positive
Activation energy, E_a near 296 K (in eV)	0.102
Energy gap estimated from the above activation energy ($2E_a$) near 296 K (in eV)	0.20
Optical energy gap E_g at 296 K(in eV)	Not detected. The sample remains nontransparent to radiation of energies down to 0.1 eV
Calculated energy gap E_g at 296 K (in eV)	0.14

carrier mobility [Fig. 9(c)] is consistent with phonon scattering mechanism for both electrons and holes ($\mu \sim T^{-3/2}$),[52,56] we considered scattering on acoustic and polar optical phonons (the scattering parameters $r_n \approx r_p$ are equal to $\sim -1/2$ and $\sim +1/2$, respectively[52]).

Using Eq. (5) for sample *A* with $S \approx -90.8$ μV/K [Fig. 11(a)], $E_g \approx 200$ meV (Fig. 8), and for the known constants ($-k/|e|$) ≈ -86.4 μV/K and $2kT \approx 50$ meV (at ambient conditions), we can estimate the partial conductivities, σ_n/σ (σ_p/σ) = 0.617 (0.383) and $\mu_n/\mu_p = 1.61$ for $r = -1/2$, and σ_n/σ (σ_p/σ) = 0.596 (0.404) and $\mu_n/\mu_p = 1.47$ for $r = +1/2$. These values are in reasonable agreement with those in the previous Sec. 2 b. (Table III). In the case of one-band conductivity the thermopower data also would permit estimation of charge carrier concentration and effective mass,[58] but as shown previously, one-band approaches are not appropriate for the golden phase of Ti_2O_3.

Notice that the thermopower [Eq. (5)] together with the electrical resistivity [Eq. (1)] and the MR effect [Eq. (4)] also form a system that could be solved with respect to n_i, μ_p, and μ_n values. Since both the thermopower and Hall are differential effects that result from a competition of electron and hole partial contributions, this system is the alternative to the one in which the Hall effect [Eq. (3)] was included. Solving this system at ambient temperature, we obtain two very close sets of data: for $r = -1/2$, $n_i = 1.74 \times 10^{17}$ cm^{-3}, $\mu_p = 68.0$ $cm^2/(Vs)$, and $\mu_n = 109.8$ $cm^2/(Vs)$; for $r = +1/2$, $n_i = 1.76 \times 10^{17}$ cm^{-3}, $\mu_p = 71.2$ $cm^2/(Vs)$, and $\mu_n = 104.9$ $cm^2/(Vs)$. The values averaged between these two sets are summarized in Table III. Neglecting the last term in Eq. (5) does not lead to any noticeable variation in the results. These values of the hole and electron mobility are a bit different than those estimated in the previous paragraph, b (Table III).

Taking into account the tiny positive (zero-like) Hall coefficient in sample *B* [Fig. 9(a)], one could expect small and likely positive thermopower values in sample *B*. However, the thermopower studies reveal a different picture: microscopic plates randomly cut from interiors of sample *B* showed piece-to-piece huge fluctuations in values and signs of the thermopower [examples are shown in Fig. 11(b)]. This finding gives an unambiguous evidence of competition between the electron and hole contributions in electrical conductivity [Eq. (5)]. We still noticed a tendency to positive thermopower values. These huge fluctuations in thermopower might suggest that sample *B* contains extended areas of *p*- and *n*-types of conductivity rather than consisting of randomly distributed microscopic grains of *p*- and *n*-types [inset in Fig. 11(b)]. A value of thermopower of each plate microsample integrates contributions of all grains from its interiors with account for their volumes, thermal conductivities, and geometrical configuration parameters.[59] Thus, sample *B* has the inhomogeneous domain structure, and, unlike sample *A*, it is not suitable for the study of intrinsic semiconducting properties of the golden phase.

3. *Electronic band structure of the golden phase of Ti_2O_3*

Based on the well-refined Th_2S_3-type structure of the golden phase (Fig. 4, Table II), we calculated an electronic band structure and density of states (Fig. 12). One can clearly see the existence of a small indirect gap. With $E_g \sim 0.14$ eV this gap is just between the values estimated from electrical resistivities for samples *A* ($E_g \sim 0.2$ eV) and *B* ($E_g \sim 0.1$ eV). Around the Fermi energy, Ti-3d electron states dominate, while O-2p electron states dominate in the energy range from -9.0 eV to -3 eV. The electronic structure of Ti_2O_3 shows a weak hybridization between the Ti-3d and the O-2p states. In these calculations we treated effects of exchange and correlation by the GGA.[20] Recently, this approach proved its efficiency in simulation of properties of titanium oxides, e.g., it could reproduce the known scenario of the pressure-driven phase transitions in TiO_2.[21] Thus, the predicted band gap value seems to be reasonable but probably underestimated.

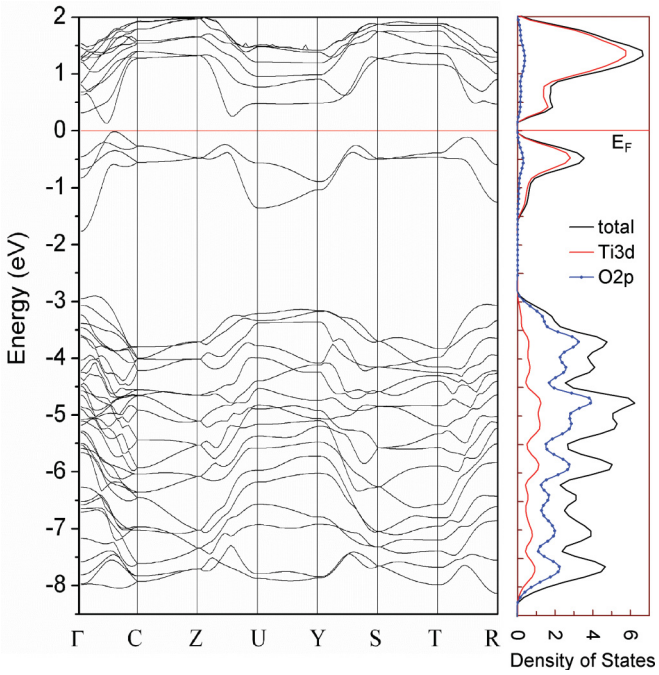

FIG. 12. (Color online) Calculated electronic band structure and density of states of the golden phase of Ti_2O_3. These data indicate that the golden phase of Ti_2O_3 is an indirect gap semiconductor with gap value of about $E_g \sim 0.14$ eV.

Besides the existence of the fundamental semiconductor band gap, the simulated band structure of the Th_2S_3-structured Ti_2O_3 shows other exciting features, e.g., nearly direct energy gaps of ∼1.8 eV between the flat top of the valence band and the flat bottom of the conductance band in the regions between C and Z and between S and T points of the Brillouin zone (Fig. 12). Hence, excitation with energy exceeding ∼2 eV could stimulate interband transition from the top of the valence band to non-occupied levels at the conduction band. This transition should be significant and well observable since the aforementioned electronic states correspond to the maxima of the density of states (right plot in Fig. 12). The reflectance and absorption study on the golden Ti_2O_3 in fact detected some absorption edge near 2.25 eV (Fig. 7). This absorption edge could explain the golden color of the material, and potentially it might be related to the above-discussed interband transition.

The golden high-pressure phase of Ti_2O_3[6,7] is not an electronic analogue of the known golden high-pressure phase of SmS.[60–65] At ambient conditions the golden phase in SmS has a tiny pseudogap of about 0.01 eV and exhibits metal-like electrical conductivity ($\rho \sim 0.3$–0.4 mΩ × cm at ambient conditions).[60–62] Likewise, the golden phase in Ti_2O_3 has the real band gap of about ∼0.2 eV (Table III) and exhibits apparently semiconducting electrical conductivity ($\rho \sim 0.20$–0.46 Ω × cm at ambient conditions) (Fig. 8). The nature of the pressure-driven structural transitions that lead to the golden phases in SmS and Ti_2O_3 is also different. The transition in SmS is isostructural: a shift in the cation valence from Sm^{2+} to Sm^{3+} leads to both rising in charge carrier concentration and shrinkage in the unit cell volume of the original NaCl-structured lattice.[63,64] It is interesting to note that the pressure-driven transition in SmS from the conventional black phase to the golden phase is accompanied by an inversion of the dominant type of electrical conductivity from *n*- and *p*-.[65] In Ti_2O_3 the transition to the golden phase occurs as a reconstructive one.[6,7]

The unusual transport and optical properties and the golden color of the golden SmS were addressed to excitonic conductivity.[63] The structural model of the Th_2S_3-type phase has only two independent crystallographic sites for the Ti ions (Fig. 4, Table II). The charge balance suggests that the Ti ions occupying both of the crystallographic sites have, likely, the oxidation state of +3. However, one can not rule out the existence of the Ti^{4+} and Ti^{2+} cations that could influence the properties of Ti_2O_3. Sitting of the Ti^{4+} ions on the sites for Ti^{3+} ones would lead to slight structural distortions, and the released electrons might remain partially delocalized, forming exciton states, rather than contribute to formation of the Ti^{2+} ions. The exciton states lying in the forbidden gap could potentially explain the reduced effective energy gap found in sample *B* (Fig. 8). Further investigations could shed a light on this issue. Comparing the carrier concentrations at ambient conditions in the golden phase of SmS ($p \sim 10^{20}$ cm^{-3})[65] and in sample *A* of Ti_2O_3 ($n \sim 10^{17}$ cm^{-3}) (Table III), one may conclude that all the above issues could not affect noticeably the previously estimated band structure parameters of sample *A*.

IV. CONCLUSION

In this work we carried out investigations of HP-HT conditions of synthesis of the golden Th_2S_3-type phase of Ti_2O_3. For the first time a *P*-*T* phase diagram of Ti_2O_3 was proposed. Based on the electronic transport studies we established that an electronic band structure of the golden phase of Ti_2O_3 corresponds well to a model of a narrow-gap semiconductor with energy gap of $E_g \sim 0.1$–0.2 eV and competing electron and hole contributions to the electrical conductivity. For sample *A* demonstrating a dominating intrinsic conductivity, we estimated a set of basic band structure parameters (e.g., carrier concentration and mobility). Meanwhile, the oxidation state of the Ti ions in the golden phase may further affect this model. In optical reflectance and absorption studies we detected an absorption edge near 2.3 eV that could originate from some interband transition. This fact can explain the unusual golden color of the Th_2S_3-type polymorph. In summary, the case of the golden oxide shows that properties and potential of even simple binary oxide systems are not yet properly understood.

ACKNOWLEDGMENTS

The authors are grateful to L. Dubrovinsky (BGI) and N. Dubrovinskaia (Universität Bayreuth) for stimulating discussions and to J. Wosnitza (Helmholtz-Zentrum, Dresden) for reading the manuscript and commenting on it. The authors thank A. V. Kurnosov (BGI), D. M. Trots (BGI), V. Dmitriev (ESRF), and H. Keppler (BGI) for help in some experiments. SVO also thanks Alexander von Humboldt Foundation and the DFG (project OV-110/1-1) for the financial support. Part of this work was partly supported by the RFBR (Grant No. 10-08-00945).

*Corresponding author: sergey.ovsyannikov@uni-bayreuth.de

[1] S. H. Shim, T. S. Duffy, R. Jeanloz, C. S. Yoo, and V. Iota, Phys. Rev. B **69**, 144107 (2004).
[2] S. Ono, T. Kikegawa, and Y. Ohishi, J. Phys. Chem. Solids **65**, 1527 (2004).
[3] S. Ono and Y. Ohishi, J. Phys. Chem. Solids **66**, 1714 (2005).
[4] A. R. Oganov and S. Ono, Proc. Nat. Acad. Sci. **102**, 10828 (2005).
[5] K. Umemoto and R. M. Wentzcovitch, Proc. Nat. Acad. Sci. **105**, 6526 (2008).
[6] D. Nishio-Hamane, M. Katagiri, K. Niwa, A. Sano-Furukawa, T. Okada, and T. Yagi, High Press. Res. **29**, 379 (2009).
[7] S. V. Ovsyannikov, X. Wu, V. V. Shchennikov, A. E. Karkin, N. Dubrovinskaya, G. Garbarino, and L. Dubrovinsky, J. Phys.: Condens. Matter **22**, 375402 (2010).
[8] A. Gurlo, D. Dzivenko, P. Kroll, and R. Riedel, Phys. Status Solidi-RRL **2**, 269 (2008).
[9] H. Yusa, T. Tsuchiya, J. Tsuchiya, N. Sata, and Y. Ohishi, Phys. Rev. B **78**, 092107 (2008).
[10] H. Yusa, T. Tsuchiya, N. Sata, and Y. Ohishi, Inorg. Chem. **48**, 7537 (2009).
[11] H. Yusa, T. Tsuchiya, N. Sata, and Y. Ohishi, Inorg. Chem. **49**, 4478 (2010).
[12] J. Liu, L. Dubrovinsky, T. Boffa Ballaran, and W. Crichton, High Press. Res. **27**, 483 (2007).
[13] M. Pagannone and H. G. Drickamer, J. Chem. Phys. **43**, 2266 (1965).
[14] D. J. Frost, B. T. Poe, R. G. Trønnes, C. Liebske, A. Duba, and D. C. Rubie, Phys. Earth Planet. Inter. **143–144**, 507 (2004).
[15] S. V. Ovsyannikov and L. Dubrovinsky, High Press. Res. **31**, 23 (2011).
[16] V. V. Shchennikov, S. V. Ovsyannikov, A. E. Karkin, S. Todo, and Y. Uwatoko, Solid State Commun. **149**, 759 (2009).
[17] V. V. Shchennikov, S. V. Ovsyannikov, and A. Y. Manakov, J. Phys. Chem. Solids **71**, 1168 (2010).
[18] G. Kresse and J. Furthmüller, Phys. Rev. B **54**, 11169 (1996).
[19] F. Birch, Phys. Rev. **71**, 809 (1947).
[20] J. P. Perdew, K. Burke, and M. Ernzerhof, Phys. Rev. Lett. **77**, 3865 (1996).
[21] X. Wu, E. Holbig, and G. Steinle-Neumann, J. Phys.: Condens. Matter **22**, 295501 (2010).
[22] F. J. Morin, Phys. Rev. Lett. **3**, 34 (1959).
[23] J. M. Honig and T. B. Reed, Phys. Rev. **174**, 1020 (1968).
[24] J. Yahia and H. P. R. Frederikse, Phys. Rev. **123**, 1257 (1961).
[25] H. L. S. Chen and R. J. Sladek, Phys. Rev. B **18**, 6824 (1978).
[26] C. N. R. Rao, R. E. Loehman, and J. M. Honig, Phys. Lett. A **27**, 271 (1968).
[27] L. J. Eckert and R. C. Bradt, J. Appl. Phys. **44**, 3470 (1973).
[28] C. E. Rice and W. R. Robinson, Acta Cryst. B **33**, 1342 (1977).
[29] B. Viswanathan, S. Usha Devi, and C. N. R. Rao, Pramana **1**, 48 (1973).
[30] R. J. Nemanich, C. C. Tsai, and G. A. N. Connell, Phys. Rev. Lett. **44**, 273 (1980).
[31] A. Mooradian and P. M. Raccah, Phys. Rev. B **3**, 4253 (1971).
[32] S. H. Shin, R. L. Aggarwal, B. Lax, and J. M. Honig, Phys. Rev. B **9**, 583 (1974).
[33] M. E. Straumanis and T. Ejima, Acta Cryst. **15**, 404 (1962).
[34] X. Wu, G. Steinle-Neumann, O. Narygina, I. Kantor, C. McCammon, V. Prakapenka, V. Swamy, and L. Dubrovinsky, Phys. Rev. Lett. **103**, 065503 (2009).
[35] D. Nishio-Hamane, T. Yagi, M. Ohshiro, K. Niwa, T. Okada, and Y. Seto, Phys. Rev. B **82**, 092103 (2010).
[36] T. Okada, T. Yagi, and D. Nishio-Hamane, Phys. Chem. Miner. **38**, 251 (2011).
[37] N. Kawai and S. Mochizuki, Phys. Lett. A **36**, 54 (1971).
[38] E. Knittle and R. Jeanloz, Solid State Commun. **58**, 129 (1986).
[39] M. P. Pasternak, G. Kh. Rozenberg, G. Yu. Machavariani, O. Naaman, R. D. Taylor, and R. Jeanloz, Phys. Rev. Lett. **82**, 4663 (1999).
[40] I. G. Austin, Philos. Mag. **7**, 961 (1962).
[41] D. B. McWhan and T. M. Rice, Phys. Rev. Lett. **22**, 887 (1969).
[42] S. A. Carter, T. F. Rosenbaum, M. Lu, H. M. Jaeger, P. Metcalf, J. M. Honig, and J. Spalek, Phys. Rev. B **49**, 7898 (1994).
[43] M. Takigawa, E. T. Ahrens, and Y. Ueda, Phys. Rev. Lett. **76**, 283 (1996).
[44] P. Limelette, A. Georges, D. Jerome, P. Wzietek, P. Metcalf, and J. M. Honig, Science **302**, 89 (2003).
[45] K. E. Smith and V. E. Henrich, Phys. Rev. B **38**, 5965 (1988).
[46] A. I. Poteryaev, A. I. Lichtenstein, and G. Kotliar, Phys. Rev. Lett. **93**, 086401 (2004).
[47] F. Rodolakis, P. Hansmann, J.-P. Rueff, A. Toschi, M. W. Haverkort, G. Sangiovanni, A. Tanaka, T. Saha-Dasgupta, O. K. Andersen, K. Held, M. Sikora, I. Alliot, J.-P. Itie, F. Baudelet, P. Wzietek, P. Metcalf, and M. Marsi, Phys. Rev. Lett. **104**, 047401 (2010).
[48] V. M. Asnin and A. A. Rogachev, Phys. Status Solidi **20**, 755 (1967).
[49] T. Shiraishi, Y. Takuma, E. Miura, Y. Tanaka, and K. Hisatsune, J. Mater. Sci.: Mater. Med. **14**, 1021 (2003), and references therein.
[50] Q. He, Q. Hao, G. Chen, B. Poudel, X. Wang, D. Wang, and Z. Ren, Appl. Phys. Lett. **91**, 052505 (2007).
[51] M. A. Afifi, M. M. Abdel-Aziz, I. S. Yahia, M. Fadel, and L. A. Wahab, J. Alloys Compd. **455**, 92 (2008).
[52] K. Seeger, *Semiconductor Physics* (Springer-Verlag, Wien, New York, 1973).
[53] M. K. Sheinkman and A. Ya. Shik, Sov. Phys. Semicond. **10**, 128 (1976).
[54] S. H. Shin, G. V. Chandrashekhar, R. E. Loehman, and J. M. Honig, Phys. Rev. B **8**, 1364 (1973).
[55] T. C. Chi and R. J. Sladek, Phys. Rev. B **7**, 5080 (1973).
[56] I. M. Tsidil'kovskii, *Thermomagnetic Phenomena in Semiconductors* (State Publ. of Phys.–Math. Lit, Moscow, 1960).
[57] V. V. Shchennikov and S. V. Ovsyannikov, Solid State Commun. **126**, 373 (2003).
[58] S. V. Ovsyannikov, V. V. Shchennikov, A. E. Karkin, A. Polian, O. Briot, S. Ruffenach, B. Gil, and M. Moret, Appl. Phys. Lett. **97**, 032105 (2010).
[59] V. V. Shchennikov, S. V. Ovsyannikov, G. V. Vorontsov, and V. V. Shchennikov Jr., Phys. Status Solidi B **241**, 3203 (2004).
[60] A. Jayaraman, V. Narayanamurti, E. Bucher, and R. G. Maines, Phys. Rev. Lett. **25**, 1430 (1970).
[61] K. Matsubayashi, K. Imura, H. S. Suzuki, G. Chen, N. Mori, T. Nishioka, K. Deguchi, and N. K. Sato, J. Phys. Soc. Jpn **76**, 033602 (2007).
[62] K. Imura, K. Matsubayashi, H. S. Suzuki, K. Deguchi, and N. K. Sato, Physica B **404**, 3028 (2009).
[63] T. Mizuno, T. Iizuka, S. Kimura, K. Matsubayashi, K. Imura, H. S. Suzuki, and N. K. Sato, J. Phys. Soc. Jpn. **77**, 113704 (2008).
[64] V. V. Kaminskii and L. N. Vasil'ev, Phys. Solid State **50**, 713 (2008).
[65] T. G. Ramesh and V. Shubha, Solid State Commun. **19**, 591 (1976).